Fourier-enhanced Implicit Neural Fusion Network for Multispectral and Hyperspectral Image Fusion

Yu-Jie Liang[†]
University of Electronic
Science and Technology of China
yujieliang0219@gmail.com

Zihan Cao[†]
University of Electronic
Science and Technology of China
iamzihan666@gmail.com

Shangqi Deng
Xi'an Jiaotong University
shangqideng0124@gmail.com

Hong-Xia Dou
Xihua University
hongxiadou1991@126.com

Liang-Jian Deng[*]
University of Electronic Science and Technology of China
liangjian.deng@uestc.edu.cn

Abstract

Recently, implicit neural representations (INR) have made significant strides in various vision-related domains, providing a novel solution for Multispectral and Hyperspectral Image Fusion (MHIF) tasks. However, INR is prone to losing high-frequency information and is confined to the lack of global perceptual capabilities. To address these issues, this paper introduces a Fourier-enhanced Implicit Neural Fusion Network (FeINFN) specifically designed for MHIF task, targeting the following phenomena: *The Fourier amplitudes of the HR-HSI latent code and LR-HSI are remarkably similar; however, their phases exhibit different patterns.* In FeINFN, we innovatively propose a spatial and frequency implicit fusion function (Spa-Fre IFF), helping INR capture high-frequency information and expanding the receptive field. Besides, a new decoder employing a complex Gabor wavelet activation function, called Spatial-Frequency Interactive Decoder (SFID), is invented to enhance the interaction of INR features. Especially, we further theoretically prove that the Gabor wavelet activation possesses a time-frequency tightness property that favors learning the optimal bandwidths in the decoder. Experiments on two benchmark MHIF datasets verify the state-of-the-art (SOTA) performance of the proposed method, both visually and quantitatively. Also, ablation studies demonstrate the mentioned contributions. The code can be available at https://github.com/294coder/Efficient-MIF.

1 Introduction

Hyperspectral imaging captures scenes across contiguous spectral bands, offering intricate details compared to traditional single or limited-band images, and improving computer vision application accuracy, such as target recognition, classification [47], tracking, and segmentation [12, 38, 39, 37, 44, 48, 49]. However, practical optical sensors face challenges in balancing spatial resolution and spectral precision. Images with over 100 bands often exhibit lower spatial resolution, while those with fewer

[†] Equal contribution.
[*] Corresponding author.

38th Conference on Neural Information Processing Systems (NeurIPS 2024).

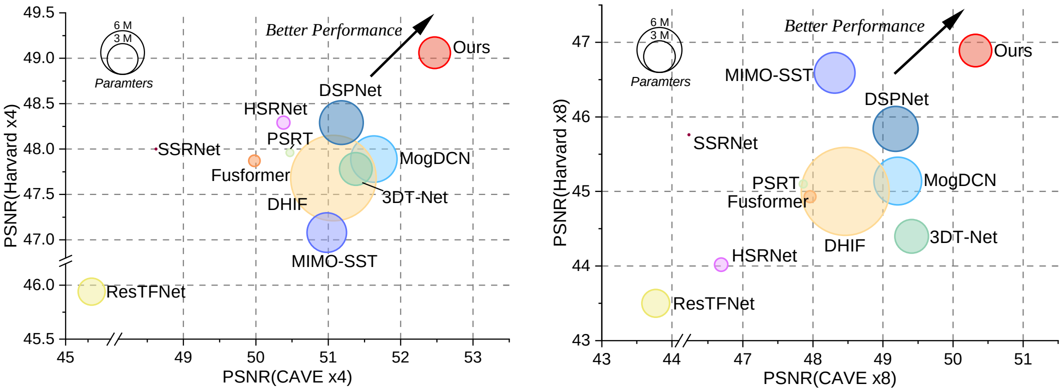

Figure 1: Comparison of our method with other methods on the CAVE($\times$ 4, $\times$ 8) and Harvard($\times$ 4, $\times$ 8) datasets. Closer to the top-right corner indicates better performance and the size of the circle indicates the number of parameters in the model.

bands display higher spatial resolution. Efforts for MHIF are underway to fuse high spatial-resolution multispectral images (HR-MSI) with low spatial-resolution hyperspectral images (LR-HSI) to finally obtain high spatial-resolution hyperspectral images (HR-HSI). Actually, MHIF technology could fuse hyperspectral images with multispectral images, extracting information not detectable by HR-MSI to enhance richness and precision. Recent MHIF literature explores model-based approaches [8, 9, 45] and deep learning methods [17, 10, 3, 54]. While model-based methods leverage image priors, challenges persist in obtaining high-fidelity, low-distortion HR-HSI due to the lack of large-scale training datasets. Among deep-learning approaches, CNN-based networks for HR-MSI and LR-HSI tend to be limited and lack interpretability for MHIF tasks and Transformer frameworks [15, 7] address the small receptive field of CNN but bring greater computational overhead.

In recent years, implicit representations of 3D scenes have garnered significant attention from researchers. For instance, Neural Radiance Field [43] models 3D static scenes by mapping coordinates to signals through a neural network. Inspired by this, researchers have revisited image representation for 2D tasks. Recent studies [5, 20, 34, 4] have achieved arbitrary-scale super-resolution (SR) by replacing commonly used upsampling layers with local implicit image functions. Though these methods demonstrate superior performance in 2D tasks, they still have some drawbacks. *Firstly*, INR calculates the RGB values of a queried coordinate based on the relative distances to the surrounding four pixels, treating it as a local operation in space that lacks consideration for global information. *Additionally*, the MLP-ReLU structure used in traditional INR inherent high-frequency information bias [29] which is challenging to be eliminated during training.

To address these issues, we propose implicit fusion functions tailored for the MHIF task as a novel fusion paradigm. We first employ encoders to extract prior information from LR-HSI and HR-MSI, which is then fed into the implicit fusion functions in the form of latent codes. Unlike traditional INR, we transform latent codes into the Fourier domain and simultaneously perform spatial and frequency fusion in a unified network. This approach not only rectifies the high-frequency insensitivity induced by the MLP but also effectively extends the receptive field, encompassing a more comprehensive scope of global information. To integrate spatial and frequency domain representations efficiently, we design a decoder with time-frequency tightness, mapping features on both domains to pixel space. The contributions of this work are three folds:

- We define a novel fusion framework based on INR, which innovatively extracts information from the spatial and Fourier domains, effectively enhances the representation ability of high-frequency information, and expands the receptive field.
- We propose a new decoder employing a Gabor wavelet activation function to enhance the interaction of INR features. Furthermore, we theoretically prove that the complex Gabor wavelet activation possesses a time-frequency tightness property, which facilitates the decoder in learning the optimal bandwidths.
- The proposed network reaches state-of-the-art (SOTA) performance on the MHIF task across two widely used hyperspectral datasets at various fusion ratios. Fig. 1 provides a fair comparison with other SOTA methods.

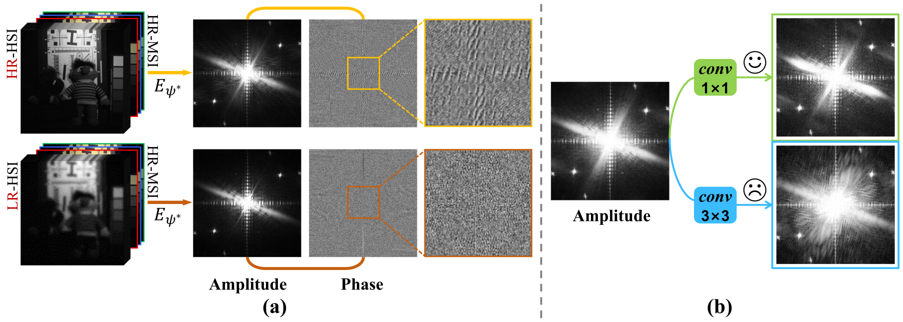

Figure 2: **(a)** The amplitude of latent code from the encoder fed by HR-HSI and LR-HSI (combined with HR-MSI) share a similarity, but the phases differ from each other. E_{ψ^*} is a trained encoder. **(b)** 3×3 convolution would suffer from the issue of spectrum leakage, which can be alleviated by 1×1 convolution.

2 Related works

Implicit Neural Representation Unlike traditional discrete representations, neural implicit representation (INR) provides a more elegant and continuous parameterized approach. Initially applied in 3D modeling tasks, NeRF [43] revolutionized 3D computer vision by representing intricate three-dimensional scenes with just 2D pose images. This line of work extends to the 2D imaging domain, where INR performs a weighted average on adjacent sub-codes to ensure output value continuity. LIIF [5] recently introduces a local implicit image function for SR, leveraging MLP to sample pixel signals across the spatial domain. Several improvements focus on decoding networks; for example, UltraSR [46] incorporates residual networks, merging spatial coordinates and depth encoding. DIINN [26] utilizes a dual-interactive implicit neural network to decouple content and position features, improving decoding capabilities. JIIF [36] proposes joint implicit image functions for multimodal learning, extracting priors from guided images. Regarding activation functions in the MLP, SIREN [34] recommends utilizing periodic activation functions for continuous INR to fit complex signals. On the other hand, WIRE [32] further employs continuous complex Gabor wavelet activation functions to activate non-linearity, focusing more on spatial frequencies. However, there is limited research dedicated to designing INR architectures specifically for the MHIF task. The unique characteristics of hyperspectral images pose challenges for INR networks, in their insensitivity to high-frequency information.

Latent Enhancement by Fourier Transform Fourier transform is a commonly used time-frequency analysis technique in signal processing, which converts signals from the time domain to the frequency domain. The Fourier domain has global statistical properties, and in recent years, many works use the Fourier transform to enhance the representation ability of neural networks. For example, FDA [53] proposes exchanging amplitude and phase components in Fourier space between images to enhance and adjust frequency information. FFC [6] introduces a novel convolution module that internally fuses cross-scale information to capture global features in Fourier space. Similarly, GFNet [30] uses 2D discrete Fourier transform to extract features, implements learnable global filtering, and replaces the self-attention layer in Transformer. UHDFour [21] embeds Fourier transform into the image enhancement network to model global information. Together, these studies demonstrate the utility of frequency domain information in improving performance on visual tasks. We exploit the architecture of FeINFN to transform latent codes into the frequency domain, implicitly integrating representations of amplitude and phase components, and enhancing high-frequency injection.

Motivation [29] finds that most neural networks exhibit a phenomenon of spectral bias through Fourier analysis. This includes neural networks such as MLP, which tend to learn low-frequency information during the early stages of training and are insensitive to high-frequency information. Moreover, we found this issue occurs in the MHIF task according to an experimental analysis as shown in Fig. 2(a), where HR-HSI and LR-HSI were concatenated with HR-MSI and fed into a trained encoder to obtain latent codes. These codes were transformed into the frequency domain to visualize the amplitude and phase. It can be observed that the amplitudes from HR-HSI and LR-HSI are very similar, while the phases differ significantly. The phase of HR-HSI should naturally contain more texture than LR-HSI, a hypothesis validated by the visualized phase maps. Based on this finding, we transformed the latent codes into the Fourier domain to separately process amplitude and phase, to enhance the global learning of high-frequency information in the images.

3 Methodology

In this section, we first present the preliminary of INR and then provide the proposed framework tailored for MHIF task. Subsequently, we elaborate on the implementation details of the composited modules of the proposed FeINFN.

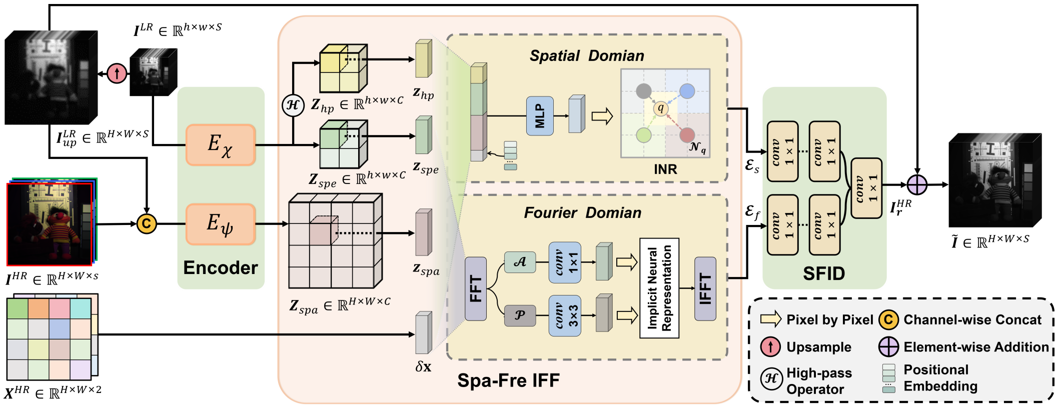

$I^{LR} \in \mathbb{R}^{h\times w\times S}$
$I^{LR}_{up} \in \mathbb{R}^{H\times W\times S}$
$I^{HR} \in \mathbb{R}^{H\times W\times s}$
$X^{HR} \in \mathbb{R}^{H\times W\times 2}$
E_χ
E_ψ
Encoder
$Z_{hp} \in \mathbb{R}^{h\times w\times C}$
$Z_{spe} \in \mathbb{R}^{h\times w\times C}$
$Z_{spa} \in \mathbb{R}^{H\times W\times C}$
z_{hp}
z_{spe}
z_{spa}
δx
Spatial Domian
MLP
q
$\mathcal{N}_q$
INR
Fourier Domian
FFT
$\mathcal{A}$
$\mathcal{P}$
conv 1×1
conv 3×3
Implicit Neural Representation
IFFT
Spa-Fre IFF
$\mathcal{E}_s$
$\mathcal{E}_f$
conv 1×1
conv 1×1
conv 1×1
conv 1×1
conv 1×1
SFID
I^{HR}_r
$\tilde{I} \in \mathbb{R}^{H\times W\times S}$
Pixel by Pixel
Channel-wise Concat
Upsample
Element-wise Addition
High-pass Operator
Positional Embedding

Figure 3: The flowchart of the FeINFN framework which is composed of a spectral encoder E_χ, a spatial encoder E_ψ, MHIF task-designed spatial and Fourier domains implicit fusion functions, and a pixel space mapping decoder. Please note that $\mathbf{I}^{LR}$ is the LR-HSI, $\mathbf{I}^{HR}$ is the HR-MSI, $\mathbf{I}^{LR}_{up}$ is the bicubic interpolation LR-HSI, and $\mathbf{X}^{HR}$ is the HR normalized 2D coordinate map. $\mathbf{z}_{spe}$, $\mathbf{z}_{spa}$, $\mathbf{z}_{hp}$, $\delta\mathbf{x}$ correspond to individual pixel units, $\mathcal{A}$ and $\mathcal{P}$ represents amplitude and phase, respectively.

3.1 Preliminary: Implicit Neural Representation

Neural Radiance Fields [43] is represented by integral construction scenes. The value of a pixel in a certain viewing angle image is regarded as the integral of the characteristics of the sampling point from the proximal end to the far end of the ray. During actual training, the integral needs to be discretized. Extended to 2D image representation [5], it is sampled pixel by pixel from the vicinity of the query target. Taking the low-resolution (LR) image $\mathbf{I} \in \mathbb{R}^{h\times w\times 3}$ upsampling to the high-resolution (HR) image $\hat{\mathbf{I}} \in \mathbb{R}^{H\times W\times 3}$ as an example, the process of generating the RGB values of the target coordinates $\mathbf{x}_q \in \mathbb{R}^2$ can be regarded as interpolation form, expressed as:

$$\hat{\mathbf{I}}(\mathbf{x}_q) = \sum_{i\in\mathcal{N}_q} w_{q,i}\mathbf{v}_{q,i}, \tag{1}$$

where $\mathbf{v}_{q,i} \in \mathbb{R}^{4\times 4\times 3}$ is the interpolation pixel of i interpolated by q's surrounding pixels $\mathcal{N}_q \in \mathbb{R}^4$ and $w_{q,i} \in \mathbb{R}$ signifies the interpolation weight. In the implicit representation of local image features, the weights $w_{q,i} = S_i/S$, where S_i represents the area formed by q and i in the diagonal region and S denotes the total area enclosed by the set $\mathcal{N}_q$. The interpolation value $\mathbf{v}_{q,i}$ is effectively generated by a basis function:

$$\mathbf{v}_{q,i} = \phi_\theta(\mathbf{z}_i, \mathbf{x}_q - \mathbf{x}_i), \tag{2}$$

where ϕ_θ is typically an MLP, $\mathbf{z}_i$ is the latent code generated by an encoder for the coordinates $\mathbf{x}_i$, and $\mathbf{x}_q - \mathbf{x}_i$ represents the relative coordinates. From the above equations, it can be inferred that the interpolation features can be represented by a set of local feature vectors in the LR domain. Typically, interpolation-based methods [28, 18] achieve upsampling by querying $\mathbf{x}_q - \mathbf{x}_i$ in the arbitrary SR task. See more details in [5].

3.2 Overview of the FeINFN Framework

In this work, we propose the FeINFN, which adopts a novel framework for simultaneously performing neural implicit representation in both the spatial and frequency domains to execute the MHIF task. Fig. 3 provides an overview of the proposed framework, designed to fuse LR-HSI $\mathbf{I}^{LR} \in \mathbb{R}^{h\times w\times S}$ and HR-MSI $\mathbf{I}^{HR} \in \mathbb{R}^{H\times W\times s}$ to generate HR-HSI $\widetilde{\mathbf{I}} \in \mathbb{R}^{H\times W\times S}$ based on a upsampling scale r.

Initially, the LR-HSI is fed into encoder E_χ to extract spectral features $\mathbf{Z}_{spe} \in \mathbb{R}^{h\times w\times C}$. Simultaneously, the concatenated bicubic interpolation LR-HSI $\mathbf{I}^{LR}_{up} \in \mathbb{R}^{H\times W\times S}$ and $\mathbf{I}^{HR}$, are fed into encoder E_ψ to extract spatial features $\mathbf{Z}_{spa} \in \mathbb{R}^{H\times W\times C}$. Additionally, the pixel's central position is represented as the coordinate point. The coordinate map is normalized into a two-dimensional grid $[-1, 1] \times [-1, 1]$, obtaining a HR normalized 2D coordinate map $\mathbf{X}^{HR} \in \mathbb{R}^{H\times W\times 2}$. The extracted $\mathbf{Z}_{spe}$ and $\mathbf{Z}_{spa}$, along with the 2D coordinates of $\mathbf{I}^{HR}$, are forwarded to Spatial-Frequency Implicit Fusion Function (Spa-Fre IFF), outputting spatial domain features $\mathcal{E}_s \in \mathbb{R}^{H\times W\times S}$ and frequency domain features $\mathcal{E}_f \in \mathbb{R}^{H\times W\times S}$. The $\mathcal{E}_s$ and $\mathcal{E}_f$ as inputs to a pixel space mapping decoder which generates the residual image $\mathbf{I}^{HR}_r \in \mathbb{R}^{H\times W\times S}$. Finally, the residual image $\mathbf{I}^{HR}_r$ is combined with the bicubicly upsampled image $\mathbf{I}^{LR}_{up}$ via element-wise addition, yielding the ultimate fusion image $\widetilde{\mathbf{I}}$.

3.3 INR Encoder Networks

Analogous to local implicit representation functions [5, 20, 34, 4], the initial step involves extracting latent code representations. For the MHIF task, we address the challenges of both upsampling and fusion simultaneously, employing implicit neural representations as the solution.

The INR encoders try to extract spatial and spectral latent codes $\mathbf{Z}_{spa} \in \mathbb{R}^{H\times W\times C}$, $\mathbf{Z}_{spe} \in \mathbb{R}^{h\times w\times C}$: one is extracted from $\mathbf{I}^{LR}$, serving as the carrier for spectral information; the other is encoded from the concatenation of $\mathbf{I}^{LR}_{up}$ and $\mathbf{I}^{HR}$, aiding in spatial information during the fusion process. This process can be denoted as:

$$\mathbf{Z}_{spe} = E_\chi(\mathbf{I}^{LR}), \quad \mathbf{Z}_{spa} = E_\psi\left(\mathrm{Cat}(\mathbf{I}^{LR}_{up}, \mathbf{I}^{HR})\right), \tag{3}$$

where E_χ is the spectral encoder parameterized by χ, E_ψ is the spatial encoder parameterized by ψ, and $\mathrm{Cat}(\mathbf{I}^{LR}_{up}, \mathbf{I}^{HR})$ denotes the concatenation along the channel dimension. In practice, we utilize EDSR [23] as INR encoder networks.

3.4 Spatial-Frequency Implicit Fusion Function

To address the mentioned issues 2, we propose Spatial-Frequency Implicit Fusion Function, dubbed Spa-Fre IFF which is a dual-branch fusion function and utilized for computing the fusion feature of $\mathbf{Z}_{spe}$ and $\mathbf{Z}_{spa}$ in the spatial and frequency domains, respectively. Given a queried HR coordinate $\mathbf{x}_q \in \mathbf{X}^{HR}$ of a pixel unit q, Spa-Fre IFF estimates spatial feature vector $\boldsymbol{\varepsilon}_s \in \mathbb{R}^{1\times 1\times S}$ ($\boldsymbol{\varepsilon}_s \in \mathcal{E}_s$) and frequency feature vector $\boldsymbol{\varepsilon}_f \in \mathbb{R}^{1\times 1\times S}$ ($\boldsymbol{\varepsilon}_f \in \mathcal{E}_f$) as follows:

$$\boldsymbol{\varepsilon}_s, \boldsymbol{\varepsilon}_f = \text{Spa-Fre IFF}(\mathbf{z}_{spe}, \mathbf{z}_{spa}, \delta\mathbf{x}), \tag{4}$$

where $\mathbf{z}_{spe} \in \mathbb{R}^{1\times 1\times C}$ represents the spectral latent code vector corresponding to $\mathbf{x}_q$, and $\mathbf{z}_{spa} \in \mathbb{R}^{4\times 4\times C}$ is the spatial latent code vector. $\delta\mathbf{x}$ denotes the set of local relative coordinates, expressed by the following formula:

$$\delta\mathbf{x} = \{\mathbf{x}_q - \mathbf{x}_{q,i}\}_{i\in\mathcal{N}_q}, \tag{5}$$

where $\mathbf{x}_{q,i}$ refers to the coordinates most proximate to the query coordinate $\mathbf{x}_q$, representing the four corner pixels closest to q in the HR space.

Spatial Implicit Fusion Function The Spatial Implicit Fusion Function aims to leverage the powerful representation capabilities of INR to achieve implicit fusion in the spatial domain, as shown in Fig. 3 (see branch "Spatial Domain"). Specifically, we employ high-pass operators $\mathcal{H}$ to filter the spectral latent codes, as a complement to the high-frequency information on the spectrum:

$$\mathbf{z}_{hp} = \mathcal{H}(\mathbf{z}_{spe}), \tag{6}$$

where $\mathbf{z}_{hp} \in \mathbb{R}^{1\times 1\times C}$ represents the high-frequency latent code of $\mathbf{I}^{LR}$. Also, we suggest frequency encoding for relative positional coordinates as follows:

$$\gamma(\delta\mathbf{x}) = [\sin(2^0\delta\mathbf{x}), \cos(2^0\delta\mathbf{x}), \cdots, \sin(2^{L-1}\delta\mathbf{x}), \cos(2^{L-1}\delta\mathbf{x})], \tag{7}$$

where L is a hyperparameter, in practice, we set L to 10. Additionally, leveraging the graph attention mechanism [36], we parameterize the solution for interpolation weights $\mathbf{w}_{q,i} \in \mathbb{R}^{1\times S}$, and the implicit fusion function simultaneously outputs fusion interpolation values $\mathbf{v}_{q,i} \in \mathbb{R}^{4\times4\times S}$ and interpolation weights $\mathbf{w}_{q,i}$. The implicit fusion function is specifically expressed as:

$$\mathbf{w}_{q,i}, \mathbf{v}_{q,i} = \phi_\theta(\mathbf{z}_{spe}, \mathbf{z}_{spa}, \mathbf{z}_{hp}, \gamma(\delta\mathbf{x})), \tag{8}$$

where ϕ_θ is an MLP parameterized by θ. The weights used for interpolation need to pass through a softmax function, obtaining normalized weights $\overline{\mathbf{w}}_{q,i}$. The spatial implicit fusion interpolation, as shown in Eq. (1), yields the fused spatial feature $\boldsymbol{\varepsilon}_s \in \mathbb{R}^{1\times1\times S}$ and can be described as follows:

$$\boldsymbol{\varepsilon}_s = \sum_{i\in\mathcal{N}_q} \overline{\mathbf{w}}_{q,i} * \mathbf{v}_{q,i}. \tag{9}$$

Frequency Implicit Fusion Function From Fig. 2(a), we observed characteristics in the frequency features between LR-HSI and HR-HSI. Hence, we design a frequency implicit fusion function to express global features continuously in the Fourier domain. Notably, directly applying static kernel convolution in the frequency domain would only enhance a specific frequency range, which is inappropriate for the fusion task. However, by learning feature content to generate weights, INR can be seen as a dynamic interpolation method in continuous space, adaptively enhancing information in the frequency domain without overly altering the frequency distribution. Therefore, introducing INR into the Fourier domain is reasonable. Since amplitude and phase exhibit different forms, as shown in Fig. 2(a), we handle them separately.

With the considerations mentioned above, as illustrated in Fig. 3 (see branch "Fourier Domain"), we initially employ FFT to transform latent codes $\mathbf{z}_{spe}$ and $\mathbf{z}_{spa}$ from the spatial domain to the frequency domain, obtaining $\mathbf{f}_{spe} \in \mathbb{R}^{1\times1\times C}$ and $\mathbf{f}_{spa} \in \mathbb{R}^{4\times4\times C}$. After the transformation, we further obtain amplitude components $\mathcal{A}(\mathbf{f}_{spe})$ and $\mathcal{A}(\mathbf{f}_{spa})$, as well as phase components $\mathcal{P}(\mathbf{f}_{spe})$ and $\mathcal{P}(\mathbf{f}_{spa})$.

For the amplitude, as shown in Fig. 2(b), the amplitude distribution of LR-HSI and HR-HSI are very similar, and the non-point-wise convolution (*e.g.* Conv 3 × 3) causes an issue of spectrum leakage, confusing channel information. In contrast, point-wise convolution does not span multiple locations in the frequency domain and has no overlap allowing it to capture information across channels effectively. Thus the fusion function for amplitude components is more suitable when applying point-wise convolution:

$$\mathbf{w}^{\mathcal{A}}_{q,i}, \mathbf{v}^{\mathcal{A}}_{q,i} = \phi^{\mathcal{A}}_\alpha(\mathcal{A}(\mathbf{f}_{spe}), \mathcal{A}(\mathbf{f}_{spa}), \delta\mathbf{x}), \tag{10}$$

where $\mathbf{w}^{\mathcal{A}}_{q,i} \in \mathbb{R}^{1\times S}$ and $\mathbf{v}^{\mathcal{A}}_{q,i} \in \mathbb{R}^{4\times4\times S}$ are the weights and interpolated values for the corresponding amplitude component, and $\phi^{\mathcal{A}}_\alpha$ is a simple network composed of two layers of point convolutions parameterized by α. Similar to operations in the spatial domain, implicit fusion interpolation is performed after obtaining interpolated values $\mathbf{v}^{\mathcal{A}}_{q,i}$ and the normalized weights $\overline{\mathbf{w}}^{\mathcal{A}}_{q,i}$:

$$\mathcal{A}'_f = \sum_{i\in\mathcal{N}_q} \overline{\mathbf{w}}^{\mathcal{A}}_{q,i} * \mathbf{v}^{\mathcal{A}}_{q,i}, \tag{11}$$

where $\mathcal{A}'_f \in \mathbb{R}^{1\times1\times S}$ is the integrated amplitude component.

For the phase, which encapsulates information such as texture details, LR-HSI and HR-HSI often have different phase information. It is known that point convolutions fail to capture sufficient spatial representations. Therefore, we use a 3 × 3 convolution to learn phase information. Additionally, small changes in the frequency domain may result in significant variations in the spatial domain. We still consider using the form of INR interpolation for phase learning. The handling of the phase components $\mathcal{P}(\mathbf{f}_{spe})$ and $\mathcal{P}(\mathbf{f}_{spa})$ are formally similar to Eqs. (10) and (11):

$$\mathbf{w}^{\mathcal{P}}_{q,i}, \mathbf{v}^{\mathcal{P}}_{q,i} = \phi^{\mathcal{P}}_\beta(\mathcal{P}(\mathbf{f}_{spe}), \mathcal{P}(\mathbf{f}_{spa}), \delta(\mathbf{x})), \quad \mathcal{P}'_f = \sum_{i\in\mathcal{N}_q} \overline{\mathbf{w}}^{\mathcal{P}}_{q,i} * \mathbf{v}^{\mathcal{P}}_{q,i}. \tag{12}$$

The simple network $\phi^{\mathcal{P}}_\beta$ consists of two layers of 3 × 3 convolutions parameterized by β. $\mathcal{P}'_f \in \mathbb{R}^{1\times1\times S}$ represents the integrated phase component.

Finally, IFFT is applied to map the frequency features $\mathcal{A}'_f$ and $\mathcal{P}'_f$ back to the image space, obtaining the frequency domain feature $\varepsilon_f \in \mathcal{E}_f$. Since in frequency space, one frequency point may correspond to multiple pixels at different positions in the spatial domain, the receptive field of INR in the frequency domain is enlarged in the spatial domain.

3.5 Spatial-Frequency Interactive Decoder

After obtaining the spatial feature map and frequency domain feature map, it is essential to consider how to integrate them seamlessly. Firstly, our decoder needs to have dual input and interactive capabilities. Secondly, it is necessary to focus on representing images in the spatial-frequency domain. With this in mind, we introduce the complex Gabor wavelet activation function with good time-frequency tightness and propose the Spatial-Frequency Interactive Decoder (SFID). Specifically, SFID consists of three layers, taking spatial and frequency domain features as inputs. The outputs $\mathbf{I}_r^{HR}$ and $\mathbf{I}_{up}^{HR}$ contribute to the final fused image $\widetilde{\mathbf{I}}$. The decoding process is illustrated in Fig. 4. The complex Gabor wavelet function is defined as:

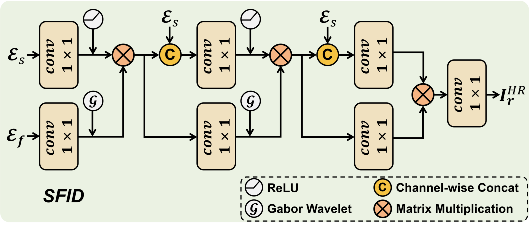

Figure 4: Detailed composition of the proposed SFID.

$$\mathcal{G}(\mathbf{x}) = e^{j\omega_0 \mathbf{x}} e^{-|\upsilon_0 \mathbf{x}|^2}, \tag{13}$$

where ω_0 is the center frequency in the frequency domain, υ_0 is a constant that is considered as the standard deviation of the Gaussian function, and $\mathbf{x}$ is a vector in the time (or spatial) domain. In what follows, we provide a theorem below that this Gabor wavelet activation has time-frequency tightness [1], which is helpful for the decoder's information interaction.

Theorem 1. *The complex Gabor wavelet activation in Eq.* (13) *has the time-frequency tightness property (more preliminary can be found in [1]). Moreover, from the perspective of signal spectrum analysis, this activation helps the decoder learn the optimal bandwidths.*

Proof: First, for the time-domas, the function $|\mathcal{G}(\mathbf{x})|$ in the time domain is primarily concentrated around $\mathbf{x} = 0$ due to the exponential decay term. The Gaussian term $e^{-|\upsilon_0 \mathbf{x}|^2}$ ensures that $\mathcal{G}(\mathbf{x})$ is bounded and rapidly decreases in the time domain. Second, for the frequency-domain Tightness, the Fourier transform is given by:

$$\mathcal{F}[\mathcal{G}(\mathbf{x})] = \int e^{j\omega_0 \mathbf{x}} e^{-|\upsilon_0 \mathbf{x}|^2} e^{-j\omega \mathbf{x}} d\mathbf{x}. \tag{14}$$

The Fourier transform of the Gaussian term $e^{-|\upsilon_0 \mathbf{x}|^2}$ remains a Gaussian function, and its bandwidth in the frequency domain is influenced by υ_0. Due to the characteristics of the Gaussian function in the frequency domain, $\mathcal{G}(\mathbf{x})$ is mainly concentrated around $\omega = \omega_0$. Combining the narrow-bandwidth properties in both time and frequency domains, we can apply the uncertainty principle to demonstrate the time-frequency tightness of the complex Gabor function:

$$|\omega_0| \cdot \upsilon_0 \geq \frac{1}{4\pi}, \tag{15}$$

where υ_0 is the time-domain bandwidth, and $|\omega_0|$ is the frequency-domain bandwidth. In practical training, we provide an initial set of bandwidths and allow the network to learn the optimal bandwidths, which concludes the proof. □

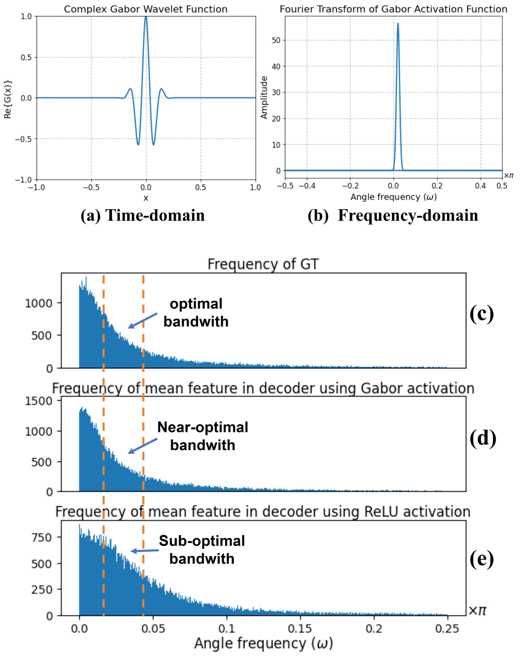

(a) Time-domain **(b) Frequency-domain**

Figure 5: **The complex Gabor wavelet function.** (a) and (b) depict the visualization of the complex Gabor wavelet function. (c), (d), and (e) represent the frequency responses of GT and decoder's mean feature using Gabor and regular ReLU activations, respectively.

As depicted in Fig. 5, the frequency response of the decoder with Gabor wavelet activation closely approximates the optimal bandwidth. Moreover, the decoder with Gabor activation achieves consistency with GT in frequency, demonstrating rapid frequency alignment.

Table 1: The average and standard deviation calculated for all the compared approaches on 11 CAVE examples and 10 Harvard examples simulating a scaling factor of 4. The best results are in bold, second-best in underline. "M" refers to millions.

Methods	CAVE ×4					Harvard ×4				
	PSNR(↑)	SAM(↓)	ERGAS(↓)	SSIM(↑)	#params	PSNR(↑)	SAM(↓)	ERGAS(↓)	SSIM(↑)	#params
Bicubic	34.33±3.88	4.45±1.62	7.21±4.90	0.944±0.029	–	38.71±4.33	2.53±0.67	4.45±1.81	0.948±0.027	–
CSTF-FUS [22]	34.46±4.28	14.37±5.30	8.29±5.29	0.866±0.075	–	39.15±3.45	6.93±2.69	4.66±1.81	0.914±0.049	–
LTTR [9]	35.85±3.49	6.99±2.55	5.99±2.92	0.956±0.029	–	40.88±3.94	4.01±1.27	4.03±2.18	0.957±0.035	–
LTMR [8]	36.54±3.30	6.71±2.19	5.39±2.53	0.963±0.021	–	42.06±3.56	3.51±0.99	3.59±2.03	0.970±0.020	–
IR-TenSR [45]	35.61±3.45	12.30±4.68	5.90±3.05	0.945±0.027	–	40.47±3.04	4.36±1.52	5.57±1.57	0.963±0.014	–
ResTFNet [24]	45.58±5.47	2.82±0.70	2.36±2.59	0.993±0.006	2.387M	45.94±4.35	2.61±0.69	2.56±1.32	0.985±0.008	2.387M
SSRNet [52]	48.62±3.92	2.54±0.84	1.63±1.21	0.995±0.002	**0.027M**	48.00±3.36	2.31±0.60	2.30±1.42	0.987±0.007	**0.027M**
HSRNet [16]	50.38±3.38	2.23±0.66	1.20±0.75	0.996±0.001	0.633M	48.29±3.03	2.26±0.56	1.87±0.81	0.988±0.006	0.633M
MogDCN [10]	51.63±4.10	2.03±0.62	1.11±0.82	0.997±0.002	6.840M	47.89±4.09	2.11±0.52	1.89±0.82	0.988±0.007	6.840M
Fusformer [15]	49.98±8.10	2.20±0.85	2.50±5.21	0.994±0.011	0.504M	47.87±5.13	2.84±2.07	2.04±0.99	0.986±0.010	0.467M
DHIF [17]	51.07±4.17	2.01±0.63	1.22±0.97	0.997±0.002	22.462M	47.68±3.85	2.32±0.53	1.95±0.92	0.988±0.007	22.462M
PSRT [7]	50.47±6.19	2.19±0.64	2.06±3.71	0.996±0.003	0.247M	47.96±3.21	2.18±0.55	1.89±0.86	0.988±0.006	0.247M
3DT-Net [25]	51.38±4.18	2.16±0.70	1.14±1.00	0.996±0.003	3.464M	47.78±4.42	**2.04±0.51**	1.98±0.86	**0.989±0.006**	3.464M
DSPNet [35]	51.18±3.92	2.15±0.64	1.13±0.82	0.997±0.002	6.064M	48.29±3.16	2.30±0.55	1.93±0.93	0.988±0.006	6.064M
MIMO-SST [11]	50.98±3.39	2.23±0.70	1.18±0.73	0.997±0.002	4.983M	47.08±5.56	2.09±0.53	2.07±0.82	0.988±0.007	4.983M
FeINFN(Ours)	**52.47±4.10**	**1.91±0.59**	**0.98±0.74**	**0.998±0.002**	3.165M	**49.06±3.15**	2.10±0.53	**1.78±0.75**	0.989±0.007	3.165M

4 Experiments

Datasets To evaluate the efficacy of our model, we conducted experiments using the CAVE and Harvard datasets. The CAVE dataset comprises 32 Hyperspectral Images (HSIs) with 31 spectral bands spanning from 400 nm to 700 nm at 10 nm intervals. We randomly selected 20 images for training and used the remaining 11 for testing. The Harvard dataset consists of 77 HSIs depicting indoor and outdoor scenes, covering the spectral range from 420 nm to 720 nm. We standardized the data by cropping the upper left sections of 20 Harvard images, with 10 for training and the rest for testing. The simulation of data can be found in Appendix.

Implementation Details We implement the proposed method FeINFN with Pytorch [27] on a workstation with an Intel I9 CPU and two 3090 GPUs. The optimizer is chosen as AdamW [19] and we use a Cosine anneal learning rate scheduler. The base channel number of the encoder is 128, that of the proposed implicit fusion function is 32 and in the decoder, the channel number is 31.

Results on CAVE Dataset In this section, we evaluate the effectiveness of FeINFN on the CAVE dataset and compare it with five traditional methods and some state-of-the-art deep learning-based approaches. As shown in Tab. 1 on the left, our method achieves optimal performance in the tasks of ×4 in all metrics. In the ×4 experiment, compared to currently leading methods such as DSPNet [35], 3DT-Net [25], and MogDCN [10], our approach demonstrates improvements in PSNR by 1.29dB/1.09dB/0.84dB, respectively. Notably, our method exhibits even more pronounced superiority in the ×8 experiment, showcasing good generalization across various resolutions. To illustrate the advantages of our method, we provide visual comparisons in Fig. 6, including close-ups and error maps to highlight specific details. Our fusion results closely match the ground truth, achieving the best quality. In comparing error maps, the darker colors indicate closer proximity to the original image. In contrast to other excellent methods, the error maps of FeINFN distinctly exhibit superior restoration effects on details.

Results on Harvard Dataset In Tab. 1, the right columns present the comparison results of our FeINFN with other methods on the Harvard dataset at scale factors 4. Our method performs exceptionally well, with only SAM being slightly surpassed by 3DT-Net [25]. FeINFN exhibits significant gains in PSNR/ERGAS metrics compared to the current state-of-the-art [16], with improvements of 0.77dB/0.09, respectively. The results with a scale factor of 8 can be found in Appendix. As depicted in Fig. 1, our model outperforms others, highlighting the crucial role of FeINFN's continuous representation capability in high-scale factor scenarios. To better visualize the performance gap, Fig. 6 illustrates the fused images and error maps, confirming that our FeINFN maintains high fidelity in recovering the texture details of the images.

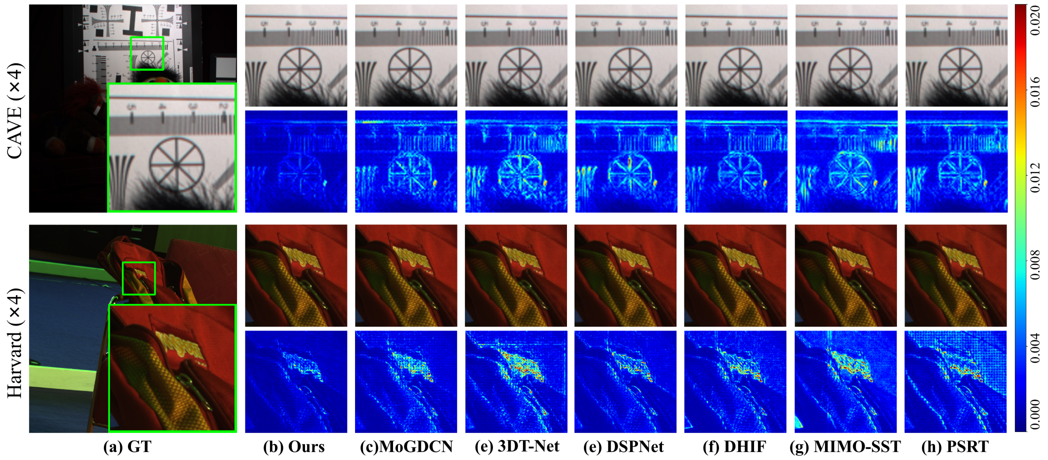

Figure 6: The upper and lower parts respectively showcase the results of "*Chart and Stuffed Toy*" from the CAVE dataset and "*Backpack*" from the Harvard dataset using pseudo-color representation. Green rectangles depict some close-up shots. The second and fourth rows show the residuals between the ground truth (GT) and the fusion products.

Table 2: Quantitative comparisons with other upsampling methods on the CAVE (×4) dataset.

Methods	PSNR(↑)	SAM(↓)	ERGAS(↓)	SSIM(↑)	#params
Bilinear	52.23±4.40	1.92±0.60	1.03±0.86	0.997±0.0021	3.119M
Bicubic	52.22±4.31	1.95±0.61	1.02±0.82	0.997±0.0021	3.119M
Pixel Shuffle	52.26±4.37	**1.90±0.59**	1.02±0.85	0.997±0.0022	3.057M
Our	**52.47±4.10**	1.91±0.59	**0.98±0.74**	**0.998±0.0015**	3.165M

Table 3: Quantitative comparisons with reduced models on the CAVE (×4) dataset. $\mathcal{S}$ & $\mathcal{F}$ mean the domain difference.

$\mathcal{S}$	$\mathcal{F}$	PSNR(↑)	SAM(↓)	ERGAS(↓)	SSIM(↑)	#params
✓	✗	52.11±4.22	1.95±0.59	1.04±0.82	0.998±0.0017	2.869M
✗	✓	47.86±3.42	3.49±1.30	1.67±1.13	0.995±0.0020	2.940M
✓	✓	**52.47±4.10**	**1.91±0.59**	**0.98±0.74**	**0.998±0.0015**	3.165M

Table 4: Quantitative comparisons with different activation functions in SFID on the CAVE (×4) dataset.

Nonlinear	PSNR(↑)	SAM(↓)	ERGAS(↓)	SSIM(↑)
ReLU	52.03±3.84	2.00±0.59	1.02±0.74	**0.998±0.0013**
GELU	51.96±3.88	2.01±0.60	1.03±0.75	0.998±0.0014
Leaky ReLU	51.98±3.92	2.01±0.60	1.03±0.76	0.998±0.0014
Our	**52.47±4.10**	**1.91±0.59**	**0.98±0.74**	0.998±0.0015

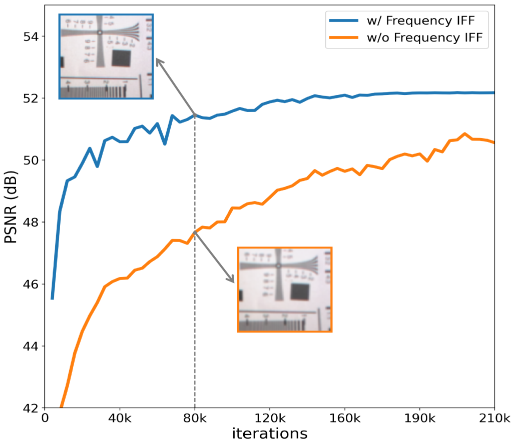

Figure 7: Changes in PSNR on the CAVE dataset of our FeINFN over iterations with and without the "Fourier Domain". The Frequency IFF can help the network learn the high-frequency details and converge faster.

4.1 Ablation Studies

Upsampling Methods Implicit image representation can be seen as an advanced interpolation algorithm, offering additional spatial information and parameterized weight generation. In this section, we compare INR with other upsampling methods. We replace INR with pixel-shuffle [33] and traditional CNN interpolation methods, presenting a comparative analysis. As seen in Tab. 2, our approach outperforms other methods in MHIF tasks.

Spatial Domain and Fourier Domain To assess the dual-domain model's efficacy, we performed model reduction, preserving spatial and Fourier domains independently. As shown in Tab. 3, FeINFN excels by using both spatial and Fourier domains concurrently, underscoring the positive impact of Fourier domain integration on overall network performance.

Spectral deviation occurs during training, where the network tends to prioritize low-frequency information, capturing high-frequency details only in later stages. To validate our resolution of this issue, we remove the "Fourier Domain" from Spa-Fre IFF, or retain it, and the corresponding training data is illustrated in Fig. 7. Our FeINFN, which incorporates Fourier domain fusion, leads to faster PSNR convergence and overall higher efficiency. The visual comparison of high-frequency details in "*chart and stuffed toy*" from the cave dataset at 80k iterations further supports the significant improvement achieved with our results.

Decoder with Different Nonlinear In this section, we evaluate the impact of different activation functions in SFID, aiming to match SFIFF. Our dual-input decoder incorporates a complex Gabor wavelet activation function to facilitate the fusion of spatial and frequency domain features.

Through experiments, we replaced the Gabor wavelet activation with other activations, presenting the results in Tab. 4. The findings distinctly demonstrate the enhanced fusion quality achieved with the complex Gabor wavelet activation. This emphasizes the critical role of wavelet activation in promoting robust and reliable learning in SFID.

5 Conclusion

Inspired by the distinct behaviors of LR-HSI and HR-HSI in the Fourier domain, we introduce a novel Fourier-enhanced Implicit Neural Fusion Network (FeINFN) based on INR. Through Fourier transformation, latent features are converted into the frequency domain, allowing the modeling of frequency components to enrich high-frequency information in images. Additionally, we propose a spatial-frequency decoding module, achieving a unified representation of both spatial and frequency domains using a time-frequency-tight activation function. Thanks to the unique design of our network, it outperforms state-of-the-art methods in MHIF with appealing efficiency. We desire that our work will inspire future research on frequency fusion-based MHIF methods.

6 Acknowledgement

This work is supported by the National Natural Science Foundation of China under Grants 12271083, 12171072 and Natural Science Foundation of Sichuan Province under Grants 2023NSFSC1341.

References

[1] Thierry Blu and Jérôme Lebrun. *Linear Time-Frequency Analysis II: Wavelet-Type Representations*, chapter 4, pages 93–130. John Wiley Sons, Ltd, 2008.

[2] Tamal Bose and Francois Meyer. *Digital signal and image processing*. John Wiley & Sons, Inc., 2003.

[3] Zihan Cao, Shiqi Cao, Liang-Jian Deng, Xiao Wu, Junming Hou, and Gemine Vivone. Diffusion model with disentangled modulations for sharpening multispectral and hyperspectral images. *Inf. Fusion.*, 104:102–158, 2024.

[4] Hao-Wei Chen, Yu-Syuan Xu, Min-Fong Hong, Yi-Min Tsai, Hsien-Kai Kuo, and Chun-Yi Lee. Cascaded local implicit transformer for arbitrary-scale super-resolution. In *IEEE/CVF Conference on Computer Vision and Pattern Recognition (CVPR)*, pages 18257–18267, 2023.

[5] Yinbo Chen, Sifei Liu, and Xiaolong Wang. Learning continuous image representation with local implicit image function. In *IEEE/CVF Conference on Computer Vision and Pattern Recognition (CVPR)*, pages 8628–8638, 2021.

[6] Lu Chi, Borui Jiang, and Yadong Mu. Fast fourier convolution. *Advances in Neural Information Processing Systems (Neurips)*, 33:4479–4488, 2020.

[7] Shang-Qi Deng, Liang-Jian Deng, Xiao Wu, Ran Ran, Danfeng Hong, and Gemine Vivone. PSRT: Pyramid shuffle-and-reshuffle transformer for multispectral and hyperspectral image fusion. *IEEE Trans. Geosci. Remote Sens.*, 61:1–15, 2023.

[8] Renwei Dian and Shutao Li. Hyperspectral image super-resolution via subspace-based low tensor multi-rank regularization. *IEEE Trans. Image Process.*, 28(10):5135–5146, 2019.

[9] Renwei Dian, Shutao Li, and Leyuan Fang. Learning a low tensor-train rank representation for hyperspectral image super-resolution. *IEEE Trans. Neural Netw. Learn. Syst.*, 30(9):2672–2683, 2019.

[10] Weisheng Dong, Chen Zhou, Fangfang Wu, Jinjian Wu, Guangming Shi, and Xin Li. Model-guided deep hyperspectral image super-resolution. *IEEE Trans. Image Process.*, 30:5754–5768, 2021.

[11] Jian Fang, Jingxiang Yang, Abdolraheem Khader, and Liang Xiao. Mimo-sst: Multi-input multi-output spatial-spectral transformer for hyperspectral and multispectral image fusion. *IEEE Trans. Geosci. Remote Sens.*, 62:1–20, 2024.

[12] Mathieu Fauvel, Yuliya Tarabalka, Jon Atli Benediktsson, Jocelyn Chanussot, and James C Tilton. Advances in spectral-spatial classification of hyperspectral images. *IEEE*, 101(3):652–675, 2012.

[13] Kaiming He, Xiangyu Zhang, Shaoqing Ren, and Jian Sun. Deep residual learning for image recognition. In *IEEE/CVF Conference on Computer Vision and Pattern Recognition (CVPR)*, pages 770–778, 2016.

[14] Alain Horé and Djemel Ziou. Image quality metrics: Psnr vs. ssim. In *International Conference on Pattern Recognition (ICIP)*, pages 2366–2369, 2010.

[15] Jinfan Hu, Tingzhu Huang, Liangjian Deng, Hongxia Dou, Danfeng Hong, and Gemine Vivone. Fusformer: A transformer-based fusion network for hyperspectral image super-resolution. *IEEE Geosci. Remote Sens. Lett.*, 19:1–5, 2022.

[16] Jinfan Hu, Tingzhu Huang, Liangjian Deng, Taixiang Jiang, Gemine Vivone, and Jocelyn Chanussot. Hyperspectral image super-resolution via deep spatiospectral attention convolutional neural networks. *IEEE Trans. Neural Netw. Learn. Syst.*, 2022.

[17] Tao Huang, Weisheng Dong, Jinjian Wu, Leida Li, Xin Li, and Guangming Shi. Deep hyperspectral image fusion network with iterative spatio-spectral regularization. *IEEE Trans. Comput Imaging.*, 8:201–214, 2022.

[18] Robert Keys. Cubic convolution interpolation for digital image processing. *IEEE Trans. Acoust. Speech Signal Process.*, 29(6):1153–1160, 1981.

[19] Diederik P Kingma and Jimmy Ba. Adam: A method for stochastic optimization. *arXiv preprint arXiv:1412.6980*, 2014.

[20] Jaewon Lee and Kyong Hwan Jin. Local texture estimator for implicit representation function. In *IEEE/CVF Conference on Computer Vision and Pattern Recognition (CVPR)*, pages 1929–1938, 2022.

[21] Chongyi Li, Chun-Le Guo, Man Zhou, Zhexin Liang, Shangchen Zhou, Ruicheng Feng, and Chen Change Loy. Embedding fourier for ultra-high-definition low-light image enhancement. In *International Conference on Learning Representations (ICLR)*, 2023.

[22] Shutao Li, Renwei Dian, Leyuan Fang, and José M Bioucas-Dias. Fusing hyperspectral and multispectral images via coupled sparse tensor factorization. *IEEE Trans. Image Process.*, 27(8):4118–4130, 2018.

[23] Bee Lim, Sanghyun Son, Heewon Kim, Seungjun Nah, and Kyoung Mu Lee. Enhanced deep residual networks for single image super-resolution. In *IEEE/CVPR Conference on Computer Vision and Pattern Recognition Workshops (CVPRW)*, pages 136–144, 2017.

[24] Xiangyu Liu, Qingjie Liu, and Yunhong Wang. Remote sensing image fusion based on two-stream fusion network. *Inf. Fusion.*, 55:1–15, 2020.

[25] Qing Ma, Junjun Jiang, Xianming Liu, and Jiayi Ma. Learning a 3d-cnn and transformer prior for hyperspectral image super-resolution. *Inf. Fusion.*, page 101907, 2023.

[26] Quan H Nguyen and William J Beksi. Single image super-resolution via a dual interactive implicit neural network. In *IEEE/CVF Winter Conference on Applications of Computer Vision (WACV)*, pages 4936–4945, 2023.

[27] Adam Paszke, Sam Gross, Francisco Massa, Adam Lerer, James Bradbury, Gregory Chanan, Trevor Killeen, Zeming Lin, Natalia Gimelshein, Luca Antiga, Alban Desmaison, Andreas Kopf, Edward Yang, Zachary DeVito, Martin Raison, Alykhan Tejani, Sasank Chilamkurthy, Benoit Steiner, Lu Fang, Junjie Bai, and Soumith Chintala. Pytorch: An imperative style, high-performance deep learning library. In *Advances in Neural Information Processing Systems (Neurips)*, pages 8024–8035. Curran Associates, Inc., 2019.

[28] William H Press. *Numerical recipes 3rd edition: The art of scientific computing*. Cambridge university press, 2007.

[29] Nasim Rahaman, Aristide Baratin, Devansh Arpit, Felix Draxler, Min Lin, Fred Hamprecht, Yoshua Bengio, and Aaron Courville. On the spectral bias of neural networks. In *International Conference on Machine Learning (ICML)*, pages 5301–5310. PMLR, 2019.

[30] Yongming Rao, Wenliang Zhao, Zheng Zhu, Jiwen Lu, and Jie Zhou. Global filter networks for image classification. *Advances in Neural Information Processing Systems (Neurips)*, 34:980–993, 2021.

[31] Dioline Sara, Ajay Kumar Mandava, Arun Kumar, Shiny Duela, and Anitha Jude. Hyperspectral and multispectral image fusion techniques for high resolution applications: A review. *Earth Science Informatics*, 14(4):1685–1705, 2021.

[32] Vishwanath Saragadam, Daniel LeJeune, Jasper Tan, Guha Balakrishnan, Ashok Veeraraghavan, and Richard G Baraniuk. Wire: Wavelet implicit neural representations. In *IEEE/CVF Conference on Computer Vision and Pattern Recognition (CVPR)*, pages 18507–18516, 2023.

[33] Wenzhe Shi, Jose Caballero, Ferenc Huszár, Johannes Totz, Andrew P Aitken, Rob Bishop, Daniel Rueckert, and Zehan Wang. Real-time single image and video super-resolution using an efficient sub-pixel convolutional neural network. In *IEEE/CVF Conference on Computer Vision and Pattern Recognition (CVPR)*, pages 1874–1883, 2016.

[34] Vincent Sitzmann, Julien Martel, Alexander Bergman, David Lindell, and Gordon Wetzstein. Implicit neural representations with periodic activation functions. *Advances in Neural Information Processing Systems (Neurips)*, 33:7462–7473, 2020.

[35] Yucheng Sun, Han Xu, Yong Ma, Minghui Wu, Xiaoguang Mei, Jun Huang, and Jiayi Ma. Dual spatial-spectral pyramid network with transformer for hyperspectral image fusion. *IEEE Trans. Geosci. Remote Sensing*, 2023.

[36] Jiaxiang Tang, Xiaokang Chen, and Gang Zeng. Joint implicit image function for guided depth super-resolution. In *Proceedings of the 29th ACM International Conference on Multimedia (ACM MM)*, pages 4390–4399, 2021.

[37] Yuliy Tarabalka, Jocelyn Chanussot, and Jón Atli Benediktsson. Segmentation and classification of hyperspectral images using minimum spanning forest grown from automatically selected markers. In *IEEE Transactions on Systems, Man, and Cybernetics (TSMC)*, volume Part B (Cybernetics) 40, pages 1267–1279, 2009.

[38] Muhammad Uzair, Arif Mahmood, and Ajmal S Mian. Hyperspectral face recognition using 3d-dct and partial least squares. In *The British Machine Vision Conference (BMVC)*, volume 1, page 10, 2013.

[39] Hien Van Nguyen, Amit Banerjee, and Rama Chellappa. Tracking via object reflectance using a hyperspectral video camera. In *IEEE Computer Society Conference on Computer Vision and Pattern Recognition-Workshops(CVPR)*, pages 44–51. IEEE, 2010.

[40] Gemine Vivone. Multispectral and hyperspectral image fusion in remote sensing: A survey. *Information Fusion*, 89:405–417, 2023.

[41] Lucien Wald. *Data fusion: definitions and architectures: fusion of images of different spatial resolutions*. Presses des MINES, 2002.

[42] Zhou Wang, Alan C Bovik, Hamid R Sheikh, and Eero P Simoncelli. Image quality assessment: from error visibility to structural similarity. *IEEE Trans. Image Process.*, 13(4):600–612, 2004.

[43] Zirui Wang, Shangzhe Wu, Weidi Xie, Min Chen, and Victor Adrian Prisacariu. NeRF–: Neural radiance fields without known camera parameters. *arXiv preprint arXiv:2102.07064*, 2021.

[44] Zhaohu Xing, Tian Ye, Yijun Yang, Guang Liu, and Lei Zhu. Segmamba: Long-range sequential modeling mamba for 3d medical image segmentation. *arXiv preprint arXiv:2401.13560*, 2024.

[45] Ting Xu, Tingzhu Huang, Liangjian Deng, and Naoto Yokoya. An iterative regularization method based on tensor subspace representation for hyperspectral image super-resolution. *IEEE Trans. Geosci. Remote Sens.*, 60:1–16, 2022.

[46] Xingqian Xu, Zhangyang Wang, and Humphrey Shi. Ultrasr: Spatial encoding is a missing key for implicit image function-based arbitrary-scale super-resolution. *arXiv preprint arXiv:2103.12716*, 2021.

[47] Yijun Yang, Huazhu Fu, Angelica I Aviles-Rivero, Carola-Bibiane Schönlieb, and Lei Zhu. Diffmic: Dual-guidance diffusion network for medical image classification. In *International Conference on Medical Image Computing and Computer-Assisted Intervention*, pages 95–105. Springer, 2023.

[48] Yijun Yang, Shujun Wang, Lei Zhu, and Lequan Yu. Hcdg: A hierarchical consistency framework for domain generalization on medical image segmentation. *arXiv preprint arXiv:2109.05742*, 2021.

[49] Yijun Yang, Zhaohu Xing, and Lei Zhu. Vivim: a video vision mamba for medical video object segmentation. *arXiv preprint arXiv:2401.14168*, 2024.

[50] Yong Yang, Lei Wu, Shuying Huang, Weiguo Wan, Wei Tu, and Hangyuan Lu. Multiband remote sensing image pansharpening based on dual-injection model. *IEEE J. Sel. Top. Appl. Earth Obs. Remote Sens.*, 13:1888–1904, 2020.

[51] Roberta H Yuhas, Alexander FH Goetz, and Joe W Boardman. Discrimination among semi-arid landscape endmembers using the spectral angle mapper (sam) algorithm. In *JPL AGW-3 Vol. 1: AVIRIS Workshop.*, 1992.

[52] Xueting Zhang, Wei Huang, Qi Wang, and Xuelong Li. SSR-NET: Spatial–spectral reconstruction network for hyperspectral and multispectral image fusion. *IEEE Trans. Geosci. Remote Sens.*, 59(7):5953–5965, 2020.

[53] Chen Zhao, Weiling Cai, Chenyu Dong, and Chengwei Hu. Wavelet-based fourier information interaction with frequency diffusion adjustment for underwater image restoration. *arXiv preprint arXiv:2311.16845*, 2023.

[54] Yu Zhong, Xiao Wu, Liang-Jian Deng, and Zihan Cao. Ssdiff: Spatial-spectral integrated diffusion model for remote sensing pansharpening. *arXiv preprint arXiv:2404.11537*, 2024.

A Appendix / supplemental material

This supplementary material provides additional insights into the background, methodologies, and experimental details outlined in our paper. It includes limitations and broader impact, experiments compute resources, details on CNNs in MHIF, 2D Fourier transform, an elucidation of the global receptive field of convolution operations within the Fourier Domain , a description of data simulation, and quality metrics. Furthermore, we present a comprehensive comparison of all methods applied to the CAVE and Harvard datasets with a scale factor of 8. This includes an ablation study, affirming the efficacy of incorporating the Fourier domain on the CAVE($\times 8$). The provided information aims to enhance the reader's understanding of the intricacies involved in our research and its practical applications.

A.1 Limitations and Broader Impact

Limitations This study has certain limitations that should be acknowledged. One primary limitation is the unavailability of ground truth (GT) data in real-world settings for the task of multispectral and hyperspectral image fusion. Due to this constraint, all datasets used in our experiments are simulated. The detailed steps for data simulation can be found in Appendix A.6. This reliance on simulated data may affect the generalizability of our results to real-world scenarios. Consequently, while our methods show promising performance in experiments, their effectiveness in practical applications remains to be fully validated. However, this limitation is a challenge faced by the entire field, not unique to our work. Surveys [40, 31] in the field of multispectral and hyperspectral image fusion highlight this common issue and discuss the need for improved data simulation methods and benchmarks.

Broader Impact This research addresses the task of multispectral and hyperspectral image fusion, which is crucial for enhancing the spatial resolution of hyperspectral images while preserving their spectral fidelity. The resulting high-resolution hyperspectral images (HR-HSI) are invaluable for various applications, such as resource monitoring, environmental management, and urban planning. In the environmental domain, fused images aid in pollution tracking, vegetation analysis, and precision agriculture, contributing to sustainable practices and environmental protection. These fused images facilitate more accurate and detailed analysis in these fields, potentially leading to better-informed decisions and more effective resource management. Despite these benefits, there are potential negative consequences to consider. Image fusion is a low-level task that significantly impacts subsequent image-processing steps. If the fusion process fails, resulting in distorted HR-HSI, it may adversely affect follow-up tasks and analyses, leading to incorrect conclusions or misguided decisions. Thus, ensuring the robustness and accuracy of the image fusion algorithm is critical to mitigating these risks.

A.2 Experiments Compute Resources

Our experiments were conducted on a workstation equipped with an Intel 12th Gen i7-12700K processor, two NVIDIA RTX 3090 GPUs, and 128GB of memory. This setup provided sufficient computational power to handle the intensive tasks involved in multispectral and hyperspectral image fusion.

A.3 Related Works: CNNs in MHIF

In recent years, CNN-based methods have exhibited significant success in the domain of multispectral and hyperspectral image fusion (MHIF). Their efficacy lies in their adeptness to extract high-level features from input data through end-to-end learning. SSRNet [52] leverages three distinct convolutional modules, w.r.t, a fusion module, a spatial edge module, and a spectral edge module, excelling in image reconstruction by associating a spatial-spectral loss function, contributing to robust learning outcomes. Similarly, ResTFNet [24] adopts residual structures and a two-stream fusion network, drawing inspiration from the extensive application of ResNet [13] in super-resolution image processing. In contrast, the MHF network [50] incorporates a well-explored linear mapping that connects HR-HSI to HR-MSI and LR-HSI, facilitating ease of interpretation. MoG-DCN [10] employs a dedicated subnet to approximate the decomposition matrix and conducts hyperspectral image super-resolution using DCN-based image regularization, leveraging prior knowledge of HSI. For the simultaneous extraction of spatial and spectral information and the acquisition of high-quality details, HSRNet [16] integrates spatial and channel attention modules, enhancing the fusion performance. However, due to the model scaling and limited convolutional receptive field, the CNN-based models still struggle to obtain satisfactory results for the MHIF task.

A.4 Preliminary: 2D Fourier Transform

Fourier transform is commonly employed in digital signal processing [2], aiming to convert signals from the time domain to the frequency domain. Through this domain transformation, previously imperceptible features often become observable. For two-dimensional images, the Fourier transform converts the signal from the spatial domain to the frequency domain, enabling the transformation of images into spectrograms in the frequency domain. Given a single-channel image $\mathbf{X} \in \mathbb{R}^{H \times W}$, the Fourier transform translates it into the Fourier space as the complex component $\mathbf{Y} \in \mathbb{C}^{H \times W}$. This process can be represented as follows:

$$\mathcal{F}(\mathbf{X})(u, v) = \mathbf{Y}(u, v) = \frac{1}{\sqrt{HW}} \sum_{h=0}^{H-1} \sum_{w=0}^{W-1} \mathbf{X}(h, w) e^{-j2\pi\left(\frac{hu}{H} + \frac{wv}{W}\right)}, \tag{16}$$

where (h, w) denotes the coordinates of $\mathbf{x}$ in the spatial space, and (u, v) represent the coordinates of $\mathbf{Y}$ in the Fourier space. The Fourier space is spanned by complex orthogonal basis functions, and each complex frequency component can be expressed as amplitude $\mathcal{A}(\mathbf{Y}(u, v))$ and phase $\mathcal{P}(\mathbf{Y}(u, v))$ components:

$$\mathcal{A}(\mathbf{Y}(u, v)) = \sqrt{\Re^2 \left\{\mathbf{Y}(u, v)\right\} + \Im^2 \left\{\mathbf{Y}(u, v)\right\}}, \tag{17}$$

$$\mathcal{P}(\mathbf{Y}(u, v)) = \arctan\left[\frac{\Im(\mathbf{Y}(u, v))}{\Re(\mathbf{Y}(u, v))}\right], \tag{18}$$

where $\Re(\mathbf{Y})$ and $\Im(\mathbf{Y})$ respectively represent the real and imaginary parts. For multi-channel images, in the utilization of the Fourier transform, we perform individual Fourier calculations for each channel. Additionally, the Fourier transform is a reversible transformation, enabling bidirectional conversion between the original signal and the transformed signal, we denote $\mathcal{F}^{-1}$ as the Fourier inverse transform.

A.5 The Receptive Field of INR in the Fourier Domain

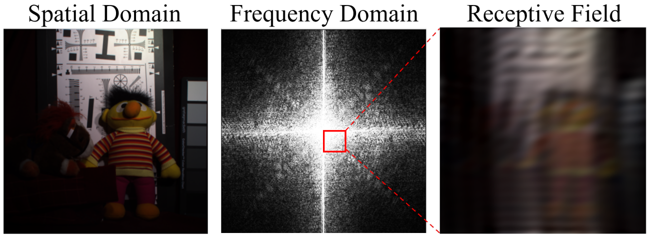

Figure 8: Convolving an image in the frequency domain is globally impactful in the spatial domain.

To validate the global nature of implicit feature fusion in the Fourier domain, we conducted experiments as illustrated in Fig. 8. We transform the "*chart and stuffed toy*" sample from the CAVE dataset into the Fourier domain, performed convolutions only on specific frequency features, and then transform it back to the spatial domain. It can be observed that Fourier domain convolution yields a global response in the spatial domain. Performing INR in the frequency domain indeed expands the receptive field of INR, freeing it from local constraints.

A.6 Data Simulation

The proposed architecture takes LR-HSI and HR-MSI pairs ($\mathbf{I}^{LR}$, $\mathbf{I}^{HR}$) as input, with the training ground-truth (GT) being HR-HSI. However, due to the unavailability of HR-HSI as a reference, a simulation phase is necessary. In our experiments using the CAVE dataset, we cropped 20 training images, generating 3920 overlapping patches of size $64 \times 64 \times 31$. These patches serve as HR-HSI (ground truth) patches. To simulate appropriate LR-HSIs, we applied a 3×3 Gaussian blur kernel

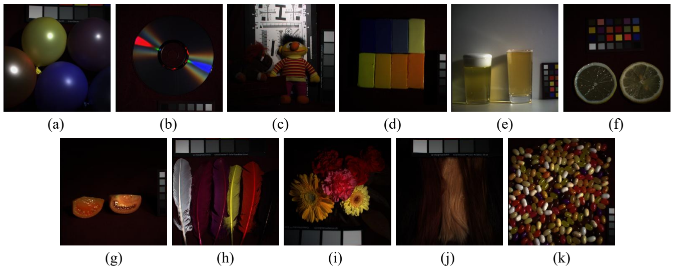

Figure 9: The testing images from the CAVE dataset: (a) *balloons*, (b) *cd*, (c) *chart and stuffed toy*, (d) *clay*, (e) *fake and real beers*, (f) *fake and real lemon slices*, (g) *fake and real tomatoes*, (h) *feathers*, (i) *flowers*, (j) *hairs*, and (k) *jelly beans*. An RGB color representation is used to depict the images.

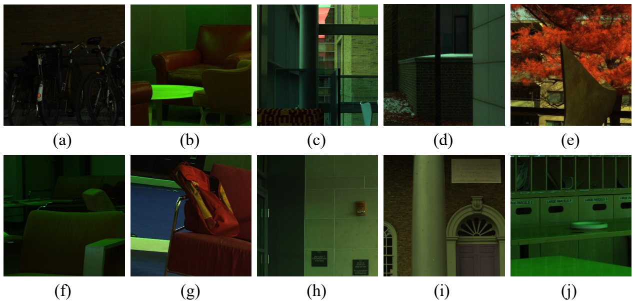

Figure 10: The 10 images tested on the Harvard dataset are (a) *bikes*, (b) *sofa1*, (c) *window*, (d) *fence*, (e) *tree*, (f) *sofa2*, (g) *backpack*, (h) *wall*, (i) *door* and (j) *parcels*.

with a standard deviation of 0.5 to the original HR-HSIs. Subsequently, we downsampled the blurred patches by a factor of 4. HR-MSI patches were generated using the spectral response function of a Nikon D700 camera. Therefore, input pairs ($\mathbf{I}^{LR}$, $\mathbf{I}^{HR}$) consist of 3920 LR-HSI patches of size $16 \times 16 \times 31$ and RGB image patches of size $64 \times 64 \times 3$. Paired with their corresponding GTs, these pairs were randomly split into training data (80%) and validation data (20%). The testing set of the CAVE dataset is shown in Fig. 9. The same procedure was employed to simulate the input LR-HSI and HR-MSI pairs and GTs for the Harvard dataset. The Harvard test set is shown in Fig. 10.

A.7 Quality Metrics

We compare our method with other methods using different image quality metrics to validate the image fusion capability of our model, including the Spectral Angle Mapper (SAM) [51], the Erreur Relative Globale Adimensionnelle de Synthèse (ERGAS) [41], the Peak Signal-to-Noise Ratio (PSNR) [14], and the Structural SIMilarity (SSIM) [42].

PSNR evaluates the spatial quality of each band in the reconstructed HR-HSI. It is calculated as follows:

$$\text{PSNR}(\mathbf{I}, \widetilde{\mathbf{I}}) = \frac{1}{B}\sum_{i=1}^{B} \text{PSNR}(\mathbf{I}^i, \widetilde{\mathbf{I}}^i), \tag{19}$$

Here, $\mathbf{I}^i \in \mathbb{R}^{H\times W}$ and $\widetilde{\mathbf{I}}^i \in \mathbb{R}^{H\times W}$ represent the i-th band of $\mathbf{I} \in \mathbb{R}^{H\times W\times B}$ and $\widetilde{\mathbf{I}} \in \mathbb{R}^{H\times W\times B}$, respectively. The PSNR function is defined as:

$$\text{PSNR}(\mathbf{I}^i, \widetilde{\mathbf{I}}^i) = 20 \cdot \log_{10}\left(\frac{\max(\mathbf{I}^i)}{\sqrt{\text{MSE}(\mathbf{I}^i, \widetilde{\mathbf{I}}^i)}}\right), \tag{20}$$

where MSE (Mean Square Error) between $\mathbf{I}^i$ and $\widetilde{\mathbf{I}}^i$, and $\max(\cdot)$ is the maximum value of $\mathbf{I}^i$.

SAM measures the spectral distortion of each hyperspectral pixel in the reconstructed HR-HSI. It is given by:

$$\text{SAM}(\mathbf{I}, \widetilde{\mathbf{I}}) = \frac{1}{HW} \sum_{i=1}^{HW} \cos^{-1} \left(\frac{\mathbf{I}_i^T \widetilde{\mathbf{I}}_i}{||\mathbf{I}_i||_2 ||\widetilde{\mathbf{I}}_i||_2} \right), \tag{21}$$

where $\cos^{-1}$ is the arccosine function, $\mathbf{I}_i \in \mathbb{R}^{B \times 1}$ and $\widetilde{\mathbf{I}}_i \in \mathbb{R}^{B \times 1}$ are the spectra of the i-th pixel of $\mathbf{I}$ and $\widetilde{\mathbf{I}}$, respectively, $|| \cdot ||_2$ is the ℓ_2 norm, and $\cdot^T$ denotes the transpose.

ERGAS measures the global statistical quality of the reconstructed HR-HSI, taking into account the ratio of the ground sample distances between HR-MSI and LR-HSI. It is formulated as:

$$\text{ERGAS}(\mathbf{I}, \widetilde{\mathbf{I}}) = \frac{100}{c} \sqrt{\frac{1}{B} \sum_{i=1}^{B} \frac{\text{MSE}(\mathbf{I}^i, \widetilde{\mathbf{I}}^i)}{\mu^2_{\widetilde{\mathbf{I}}^i}}}, \tag{22}$$

where c is the scaling factor, and $\mu^2_{\widetilde{\mathbf{I}}^i}$ is the square of the mean value of $\widetilde{\mathbf{I}}^i$.

SSIM is used to assess the structural differences between GT and the reconstructed HR-HS, incorporating both luminance and structural contrast functions. The SSIM function is defined as:

$$\text{SSIM}(\mathbf{I}, \widetilde{\mathbf{I}}) = \frac{1}{B} \sum_{i=1}^{B} \frac{(2\mu_{\mathbf{I}^i}\mu_{\widetilde{\mathbf{I}}^i} + C_1)(2\sigma_{\mathbf{I}^i\widetilde{\mathbf{I}}^i} + C_2)}{(\mu^2_{\mathbf{I}^i} + \mu^2_{\widetilde{\mathbf{I}}^i} + C_1)(\sigma^2_{\mathbf{I}^i} + \sigma^2_{\widetilde{\mathbf{I}}^i} + C_2)}, \tag{23}$$

where, B is the number of bands, and $\mathbf{I}$ and $\widetilde{\mathbf{I}}$ are sets containing $\mathbf{I}^i$ and $\widetilde{\mathbf{I}}^i$ for $i = 1$ to B, respectively. $\mu_{\mathbf{I}^i}$ and $\mu_{\widetilde{\mathbf{I}}^i}$ represent the mean values of $\mathbf{I}^i$ and $\widetilde{\mathbf{I}}^i$, while $\sigma^2_{\mathbf{I}^i}$ and $\sigma^2_{\widetilde{\mathbf{I}}^i}$ denote their variances. The term $\sigma_{\mathbf{I}^i\widetilde{\mathbf{I}}^i}$ indicates the covariance between $\mathbf{I}^i$ and $\widetilde{\mathbf{I}}^i$. Constants C_1 and C_2 are fixed values.

Higher PSNR values indicate better performance, while lower SAM and ERGAS values signify higher quality of the reconstructed HR-HSI. SSIM values range from -1 to 1, with values closer to 1 indicating better quality. Ideally, PSNR should be infinite, SAM and ERGAS should be zero, and SSIM should be one.

A.8 Benchmark

To evaluate FeINFN's performance, we compare it with MHIF methods on the CAVE and Harvard datasets. The bicubic-interpolated result of the upsampled LR-HSI in Tab. 1 serves as our baseline. Various model-based techniques, including the CSTF-FUS [22], LTTR [9], LTMR [8], and IR-TenSR [45] approaches, are considered. Additionally, we compare our approach with various deep learning methods, such as SSRNet [52], ResTFNet [24], HSRNet [16], MoGDCN [10], Fusformer [15], and DHIF [17], PSRT [7], 3DT-Net [25], DSPNet [35], MIMO-SST [11]. We compare our method with other methods using different image quality metrics to validate the image fusion capability of our model, including SAM [51], ERGAS [41], PSNR [14], and SSIM [42].

A.9 More Comparisons with the Larger Scaling Factor on CAVE and Harvard Datasets

Due to space constraints in the main text, we present a more detailed comparison of our FeINFN with other methods on four metrics for the CAVE dataset and the Harvard dataset in the supplementary material. As shown in Tab. 5, FeINFN demonstrates the best overall performance. While it ranks second in SAM on the CAVE dataset, it maintains the optimal results for other metrics.

A.10 Ablation Study: The Effectiveness of Fourier Domain Incorporation on CAVE (×8)

In the main text, we described our ablation experiments to investigate the effectiveness of incorporating the Fourier domain. Additionally, we were interested in assessing its efficacy at larger scale factors. Therefore, we applied pruning to the model on the CAVE (×8) dataset to validate its effectiveness. The experimental results, as shown in Tab. 6, indicate that the model performs best when incorporating the Fourier domain operation, aligning with our hypothesis. This provides robust evidence supporting the enhancement of network performance through INR in the Fourier domain.

Table 5: The average and standard deviation calculated for all the compared approaches on 11 CAVE examples and 10 Harvard examples simulating a scaling factor of 8. The best results are in bold, second-best in underline. "M" refers to millions.

Methods	CAVE ×8						Harvard ×8					
	PSNR(↑)	SAM(↓)	ERGAS(↓)	SSIM(↑)	#params	#flops	PSNR(↑)	SAM(↓)	ERGAS(↓)	SSIM(↑)	#params	#flops
Bicubic	29.96±3.54	5.89±2.32	5.56±3.08	0.887±0.066	–	–	33.18±6.85	3.10±0.90	3.83±1.84	0.894±0.073	–	–
CSTF-FUS [22]	38.44±4.25	7.00±2.65	2.11±1.15	0.959±0.033	–	–	39.84±6.51	4.49±1.52	2.40±1.84	0.932±0.092	–	–
LTTR [9]	37.92±3.59	5.37±1.96	2.44±1.05	0.972±0.018	–	–	42.09±4.56	3.62±1.34	1.80±0.96	0.960±0.048	–	–
LTMR [8]	38.41±3.57	5.04±1.70	2.24±0.97	0.974±0.017	–	–	42.09±4.56	3.62±1.34	1.80±0.92	0.959±0.060	–	–
IR-TenSR [45]	36.79±3.64	12.87±4.98	2.68±1.41	0.944±0.031	–	–	40.04±3.89	5.40±1.76	4.75±1.55	0.958±0.016	–	–
ResTFNet [24]	43.77±5.34	3.49±0.94	1.38±1.25	0.992±0.006	2.387M	1.75G	43.50±3.96	3.53±1.11	1.74±0.93	0.979±0.012	2.387M	1.75G
SSRNet [52]	46.23±4.19	3.13±0.97	1.05±0.73	0.993±0.004	0.446M	0.11G	45.76±3.34	2.99±0.98	1.34±0.74	0.983±0.010	0.027M	0.11G
HSRNet [16]	46.69±4.48	2.91±0.86	0.93±0.63	0.994±0.003	3.010M	2.00G	44.02±4.89	3.64±1.79	1.49±0.81	0.980±0.013	0.633M	2.00G
MogDCN [10]	49.21±4.99	2.44±0.74	0.76±0.63	**0.996±0.003**	6.840M	47.48G	45.14±5.41	3.19±1.45	1.75±1.66	0.980±0.019	7.444M	47.48G
Fusformer [15]	47.96±7.79	2.75±1.30	1.45±2.69	0.990±0.022	0.551M	9.83G	44.93±5.65	3.63±2.40	1.49±0.96	0.979±0.017	0.467M	9.83G
DHIF [17]	48.46±4.89	2.50±0.79	0.83±0.67	**0.996±0.003**	22.462M	54.27G	45.00±4.13	3.70±1.68	1.32±0.61	0.983±0.011	22.462M	54.27G
PSRT [7]	47.86±7.53	2.73±0.80	1.52±3.02	0.994±0.005	0.247M	1.14G	45.10±4.06	2.90±0.84	1.37±0.84	0.985±0.009	0.247M	1.14G
3DT-Net [25]	49.41±5.83	**2.26±0.66**	0.83±1.07	**0.996±0.003**	3.464M	68.07G	44.41±5.38	2.93±0.88	1.55±0.89	0.983±0.010	3.464M	68.07G
DSPNet [35]	49.18±4.84	2.57±0.79	0.75±0.62	**0.996±0.003**	6.064M	6.81G	45.84±3.62	2.97±0.75	1.33±0.64	0.984±0.010	6.064M	6.81G
MIMO-SST [11]	48.31±5.04	2.88±0.86	0.89±0.79	0.995±0.004	4.983M	1.58G	46.59±3.34	2.91±0.75	2.29±1.03	0.985±0.009	4.983M	1.58G
FeINFN(Ours)	**50.32± 5.17**	2.33±0.75	**0.67±0.60**	**0.996±0.003**	3.165M	10.53G	**46.89±3.59**	**2.78±0.73**	**1.16±0.57**	**0.986±0.009**	3.165M	10.53G

Table 6: The four average QIs and the corresponding parameters on the 11 testing images from the CAVE dataset simulating a scaling factor of 8. $\mathcal{S}$ & $\mathcal{F}$ means the domain difference.

$\mathcal{S}$	$\mathcal{F}$	PSNR(↑)	SAM(↓)	ERGAS(↓)	SSIM(↑)
✓	✗	50.01±5.33	2.36±0.72	0.71±0.68	0.996±0.0031
✗	✓	47.60±4.18	4.24±1.69	0.88±0.61	0.993±0.0041
✓	✓	**50.32±5.17**	**2.33±0.75**	**0.67±0.60**	**0.996±0.0028**

A.11 Ablation Study: The Effectiveness of Decoder with Complex Gabor Wavelet Activation

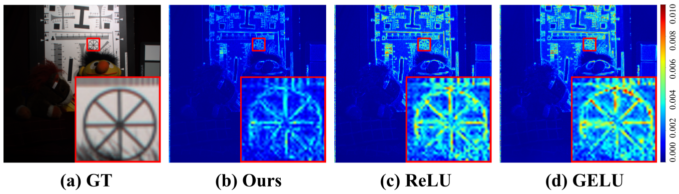

Figure 11: Error map for fusing an image with edges.

The Gabor wavelet activation demonstrates high representational power for visual signals, as depicted in Fig. 11. Compared to other activation functions, we observe that models utilizing the Gabor wavelet function exhibit lower error and spatial compactness.

NeurIPS Paper Checklist

1. **Claims**

   Question: Do the main claims made in the abstract and introduction accurately reflect the paper's contributions and scope?

   Answer: [Yes]

   Justification: The abstract and introduction clearly outline the main contributions and scope of the paper, ensuring that the claims made are supported by the theoretical and experimental results presented.

   Guidelines:

   - The answer NA means that the abstract and introduction do not include the claims made in the paper.
   - The abstract and/or introduction should clearly state the claims made, including the contributions made in the paper and important assumptions and limitations. A No or NA answer to this question will not be perceived well by the reviewers.
   - The claims made should match theoretical and experimental results, and reflect how much the results can be expected to generalize to other settings.
   - It is fine to include aspirational goals as motivation as long as it is clear that these goals are not attained by the paper.

2. **Limitations**

   Question: Does the paper discuss the limitations of the work performed by the authors?

   Answer: [Yes]

   Justification: The paper discusses the limitations in Appendix A.1, such as assumptions made in the model and potential areas where the results may not be generalized.

   Guidelines:

   - The answer NA means that the paper has no limitation while the answer No means that the paper has limitations, but those are not discussed in the paper.
   - The authors are encouraged to create a separate "Limitations" section in their paper.
   - The paper should point out any strong assumptions and how robust the results are to violations of these assumptions (e.g., independence assumptions, noiseless settings, model well-specification, asymptotic approximations only holding locally). The authors should reflect on how these assumptions might be violated in practice and what the implications would be.
   - The authors should reflect on the scope of the claims made, e.g., if the approach was only tested on a few datasets or with a few runs. In general, empirical results often depend on implicit assumptions, which should be articulated.
   - The authors should reflect on the factors that influence the performance of the approach. For example, a facial recognition algorithm may perform poorly when image resolution is low or images are taken in low lighting. Or a speech-to-text system might not be used reliably to provide closed captions for online lectures because it fails to handle technical jargon.
   - The authors should discuss the computational efficiency of the proposed algorithms and how they scale with dataset size.
   - If applicable, the authors should discuss possible limitations of their approach to address problems of privacy and fairness.
   - While the authors might fear that complete honesty about limitations might be used by reviewers as grounds for rejection, a worse outcome might be that reviewers discover limitations that aren't acknowledged in the paper. The authors should use their best judgment and recognize that individual actions in favor of transparency play an important role in developing norms that preserve the integrity of the community. Reviewers will be specifically instructed to not penalize honesty concerning limitations.

3. **Theory Assumptions and Proofs**

   Question: For each theoretical result, does the paper provide the full set of assumptions and a complete (and correct) proof?

Answer: [Yes]

Justification: For Theorem 1 presented in the paper, a complete proof is given in the main text, along with detailed explanations and illustrations.

Guidelines:

- The answer NA means that the paper does not include theoretical results.
- All the theorems, formulas, and proofs in the paper should be numbered and cross-referenced.
- All assumptions should be clearly stated or referenced in the statement of any theorems.
- The proofs can either appear in the main paper or the supplemental material, but if they appear in the supplemental material, the authors are encouraged to provide a short proof sketch to provide intuition.
- Inversely, any informal proof provided in the core of the paper should be complemented by formal proofs provided in appendix or supplemental material.
- Theorems and Lemmas that the proof relies upon should be properly referenced.

4. **Experimental Result Reproducibility**

   Question: Does the paper fully disclose all the information needed to reproduce the main experimental results of the paper to the extent that it affects the main claims and/or conclusions of the paper (regardless of whether the code and data are provided or not)?

   Answer: [Yes]

   Justification: The paper provides detailed descriptions of the network architecture and experimental settings, and the datasets used are publicly available. The complete code will be published on GitHub upon acceptance for further research and discussion.

   Guidelines:

   - The answer NA means that the paper does not include experiments.
   - If the paper includes experiments, a No answer to this question will not be perceived well by the reviewers: Making the paper reproducible is important, regardless of whether the code and data are provided or not.
   - If the contribution is a dataset and/or model, the authors should describe the steps taken to make their results reproducible or verifiable.
   - Depending on the contribution, reproducibility can be accomplished in various ways. For example, if the contribution is a novel architecture, describing the architecture fully might suffice, or if the contribution is a specific model and empirical evaluation, it may be necessary to either make it possible for others to replicate the model with the same dataset, or provide access to the model. In general. releasing code and data is often one good way to accomplish this, but reproducibility can also be provided via detailed instructions for how to replicate the results, access to a hosted model (e.g., in the case of a large language model), releasing of a model checkpoint, or other means that are appropriate to the research performed.
   - While NeurIPS does not require releasing code, the conference does require all submissions to provide some reasonable avenue for reproducibility, which may depend on the nature of the contribution. For example
     (a) If the contribution is primarily a new algorithm, the paper should make it clear how to reproduce that algorithm.
     (b) If the contribution is primarily a new model architecture, the paper should describe the architecture clearly and fully.
     (c) If the contribution is a new model (e.g., a large language model), then there should either be a way to access this model for reproducing the results or a way to reproduce the model (e.g., with an open-source dataset or instructions for how to construct the dataset).
     (d) We recognize that reproducibility may be tricky in some cases, in which case authors are welcome to describe the particular way they provide for reproducibility. In the case of closed-source models, it may be that access to the model is limited in some way (e.g., to registered users), but it should be possible for other researchers to have some path to reproducing or verifying the results.

5. **Open access to data and code**

   Question: Does the paper provide open access to the data and code, with sufficient instructions to faithfully reproduce the main experimental results, as described in supplemental material?

   Answer: [Yes]

   Justification: The datasets are publicly accessible, and the code will be released soon.

   Guidelines:

   - The answer NA means that paper does not include experiments requiring code.
   - Please see the NeurIPS code and data submission guidelines (https://nips.cc/public/guides/CodeSubmissionPolicy) for more details.
   - While we encourage the release of code and data, we understand that this might not be possible, so "No" is an acceptable answer. Papers cannot be rejected simply for not including code, unless this is central to the contribution (e.g., for a new open-source benchmark).
   - The instructions should contain the exact command and environment needed to run to reproduce the results. See the NeurIPS code and data submission guidelines (https://nips.cc/public/guides/CodeSubmissionPolicy) for more details.
   - The authors should provide instructions on data access and preparation, including how to access the raw data, preprocessed data, intermediate data, and generated data, etc.
   - The authors should provide scripts to reproduce all experimental results for the new proposed method and baselines. If only a subset of experiments are reproducible, they should state which ones are omitted from the script and why.
   - At submission time, to preserve anonymity, the authors should release anonymized versions (if applicable).
   - Providing as much information as possible in supplemental material (appended to the paper) is recommended, but including URLs to data and code is permitted.

6. **Experimental Setting/Details**

   Question: Does the paper specify all the training and test details (e.g., data splits, hyperparameters, how they were chosen, type of optimizer, etc.) necessary to understand the results?

   Answer: [Yes]

   Justification: In Sec. 4, we present the datasets and implementation details, and the simulation details of the datasets can be found in Appendix A.6.

   Guidelines:

   - The answer NA means that the paper does not include experiments.
   - The experimental setting should be presented in the core of the paper to a level of detail that is necessary to appreciate the results and make sense of them.
   - The full details can be provided either with the code, in appendix, or as supplemental material.

7. **Experiment Statistical Significance**

   Question: Does the paper report error bars suitably and correctly defined or other appropriate information about the statistical significance of the experiments?

   Answer: [No]

   Justification: The paper does not involve error bars or experiments concerning statistical significance.

   Guidelines:

   - The answer NA means that the paper does not include experiments.
   - The authors should answer "Yes" if the results are accompanied by error bars, confidence intervals, or statistical significance tests, at least for the experiments that support the main claims of the paper.

- The factors of variability that the error bars are capturing should be clearly stated (for example, train/test split, initialization, random drawing of some parameter, or overall run with given experimental conditions).
- The method for calculating the error bars should be explained (closed form formula, call to a library function, bootstrap, etc.)
- The assumptions made should be given (e.g., Normally distributed errors).
- It should be clear whether the error bar is the standard deviation or the standard error of the mean.
- It is OK to report 1-sigma error bars, but one should state it. The authors should preferably report a 2-sigma error bar than state that they have a 96% CI, if the hypothesis of Normality of errors is not verified.
- For asymmetric distributions, the authors should be careful not to show in tables or figures symmetric error bars that would yield results that are out of range (e.g. negative error rates).
- If error bars are reported in tables or plots, The authors should explain in the text how they were calculated and reference the corresponding figures or tables in the text.

8. **Experiments Compute Resources**

   Question: For each experiment, does the paper provide sufficient information on the computer resources (type of compute workers, memory, time of execution) needed to reproduce the experiments?

   Answer: [Yes]

   Justification: The compute resources for the experiments can be found in the implementation details of Sec. 4 (Experiments) and Appendix A.2.

   Guidelines:

   - The answer NA means that the paper does not include experiments.
   - The paper should indicate the type of compute workers CPU or GPU, internal cluster, or cloud provider, including relevant memory and storage.
   - The paper should provide the amount of compute required for each of the individual experimental runs as well as estimate the total compute.
   - The paper should disclose whether the full research project required more compute than the experiments reported in the paper (e.g., preliminary or failed experiments that didn't make it into the paper).

9. **Code Of Ethics**

   Question: Does the research conducted in the paper conform, in every respect, with the NeurIPS Code of Ethics https://neurips.cc/public/EthicsGuidelines?

   Answer: [Yes]

   Justification: The research adheres to the ethical guidelines set forth by NeurIPS, ensuring responsible conduct in all aspects of the study.

   Guidelines:

   - The answer NA means that the authors have not reviewed the NeurIPS Code of Ethics.
   - If the authors answer No, they should explain the special circumstances that require a deviation from the Code of Ethics.
   - The authors should make sure to preserve anonymity (e.g., if there is a special consideration due to laws or regulations in their jurisdiction).

10. **Broader Impacts**

    Question: Does the paper discuss both potential positive societal impacts and negative societal impacts of the work performed?

    Answer: [Yes]

    Justification: The broader impacts of this work can be found in Appendix A.1.

    Guidelines:

    - The answer NA means that there is no societal impact of the work performed.

- If the authors answer NA or No, they should explain why their work has no societal impact or why the paper does not address societal impact.
- Examples of negative societal impacts include potential malicious or unintended uses (e.g., disinformation, generating fake profiles, surveillance), fairness considerations (e.g., deployment of technologies that could make decisions that unfairly impact specific groups), privacy considerations, and security considerations.
- The conference expects that many papers will be foundational research and not tied to particular applications, let alone deployments. However, if there is a direct path to any negative applications, the authors should point it out. For example, it is legitimate to point out that an improvement in the quality of generative models could be used to generate deepfakes for disinformation. On the other hand, it is not needed to point out that a generic algorithm for optimizing neural networks could enable people to train models that generate Deepfakes faster.
- The authors should consider possible harms that could arise when the technology is being used as intended and functioning correctly, harms that could arise when the technology is being used as intended but gives incorrect results, and harms following from (intentional or unintentional) misuse of the technology.
- If there are negative societal impacts, the authors could also discuss possible mitigation strategies (e.g., gated release of models, providing defenses in addition to attacks, mechanisms for monitoring misuse, mechanisms to monitor how a system learns from feedback over time, improving the efficiency and accessibility of ML).

11. **Safeguards**

    Question: Does the paper describe safeguards that have been put in place for responsible release of data or models that have a high risk for misuse (e.g., pretrained language models, image generators, or scraped datasets)?

    Answer: [NA]

    Justification: The models compared in the paper have either received author permission or are publicly available. The datasets are public, and original papers are cited meticulously.

    Guidelines:

    - The answer NA means that the paper poses no such risks.
    - Released models that have a high risk for misuse or dual-use should be released with necessary safeguards to allow for controlled use of the model, for example by requiring that users adhere to usage guidelines or restrictions to access the model or implementing safety filters.
    - Datasets that have been scraped from the Internet could pose safety risks. The authors should describe how they avoided releasing unsafe images.
    - We recognize that providing effective safeguards is challenging, and many papers do not require this, but we encourage authors to take this into account and make a best faith effort.

12. **Licenses for existing assets**

    Question: Are the creators or original owners of assets (e.g., code, data, models), used in the paper, properly credited and are the license and terms of use explicitly mentioned and properly respected?

    Answer: [Yes]

    Justification: The models compared in the paper have either received author permission or are publicly available. The datasets are public, and original papers are cited meticulously.

    Guidelines:

    - The answer NA means that the paper does not use existing assets.
    - The authors should cite the original paper that produced the code package or dataset.
    - The authors should state which version of the asset is used and, if possible, include a URL.
    - The name of the license (e.g., CC-BY 4.0) should be included for each asset.

- For scraped data from a particular source (e.g., website), the copyright and terms of service of that source should be provided.
- If assets are released, the license, copyright information, and terms of use in the package should be provided. For popular datasets, paperswithcode.com/datasets has curated licenses for some datasets. Their licensing guide can help determine the license of a dataset.
- For existing datasets that are re-packaged, both the original license and the license of the derived asset (if it has changed) should be provided.
- If this information is not available online, the authors are encouraged to reach out to the asset's creators.

13. **New Assets**

    Question: Are new assets introduced in the paper well documented and is the documentation provided alongside the assets?

    Answer: [NA]

    Justification: The paper does not release new assets.

    Guidelines:

    - The answer NA means that the paper does not release new assets.
    - Researchers should communicate the details of the dataset/code/model as part of their submissions via structured templates. This includes details about training, license, limitations, etc.
    - The paper should discuss whether and how consent was obtained from people whose asset is used.
    - At submission time, remember to anonymize your assets (if applicable). You can either create an anonymized URL or include an anonymized zip file.

14. **Crowdsourcing and Research with Human Subjects**

    Question: For crowdsourcing experiments and research with human subjects, does the paper include the full text of instructions given to participants and screenshots, if applicable, as well as details about compensation (if any)?

    Answer: [NA]

    Justification: The paper does not involve crowdsourcing or research with human subjects.

    Guidelines:

    - The answer NA means that the paper does not involve crowdsourcing or research with human subjects.
    - Including this information in the supplemental material is fine, but if the main contribution of the paper involves human subjects, then as much detail as possible should be included in the main paper.
    - According to the NeurIPS Code of Ethics, workers involved in data collection, curation, or other labor should be paid at least the minimum wage in the country of the data collector.

15. **Institutional Review Board (IRB) Approvals or Equivalent for Research with Human Subjects**

    Question: Does the paper describe potential risks incurred by study participants, whether such risks were disclosed to the subjects, and whether Institutional Review Board (IRB) approvals (or an equivalent approval/review based on the requirements of your country or institution) were obtained?

    Answer: [NA]

    Justification: The paper does not involve crowdsourcing or research with human subjects.

    Guidelines:

    - The answer NA means that the paper does not involve crowdsourcing or research with human subjects.

- Depending on the country in which research is conducted, IRB approval (or equivalent) may be required for any human subjects research. If you obtained IRB approval, you should clearly state this in the paper.
- We recognize that the procedures for this may vary significantly between institutions and locations, and we expect authors to adhere to the NeurIPS Code of Ethics and the guidelines for their institution.
- For initial submissions, do not include any information that would break anonymity (if applicable), such as the institution conducting the review.